Magnetothermally-responsive nanocarriers using confined phosphorylated halloysite nanoreactor for in situ iron oxide nanoparticle synthesis: a MW-assisted solvothermal approach

José González-Rivera,[1,2] Alessio Spepi,[1] Carlo Ferrari,[2] Jorge Tovar-Rodriguez,[3] Elvira Fantechi,[1] Francesco Pineider,[1] Marco Antonio Vera-Ramírez,[4] Maria Rosaria Tiné[1*] and Celia Duce[1]

[1]Department of Chemistry and Industrial Chemistry, University of Pisa, Via G. Moruzzi 13, 56124 Pisa, Italy.

[2]National Research Council of Italy (C.N.R.), National Institute of Optics, (INO) – UOS Pisa, Via G. Moruzzi 1, 56124 Pisa, Italy.

[3]Department of Chemistry "Ugo Schiff", University of Florence, Via della Lastruccia 3, 50019 Sesto Fiorentino, Florence, Italy.

[4]Department of Chemistry, UAM-I, 55534, México D.F, 09340, México

*Email: mariarosaria.tine@unipi.it

Abstract

A family of easily recoverable magnetic and thermally responsive composite materials, with nanoscale dimensions, were synthesized by a rapid and simple solvothermal approach. The synthesis was thermally activated, accelerated, and controlled using a coaxial antenna to directly apply the microwave energy inside the solvothermal reactor. The composite materials were made up by a confined phosphorylated nanoreactor, namely halloysite nanotubes grafted on the inner lumen with phosphoric acid (HNTs-(H^+-PO_4)), that promoted the urea hydrolysis thus favoring the formation of a local alkaline environment to catalyze the homogeneous in situ precipitation of superparamagnetic iron oxide nanoparticles (IONs) selectively on their inner or outer surface. Two new MW-assisted solvothermal methodologies were used: 1) in the first the solvent is directly loaded into the MW-assisted reactor together with HNTs-(H^+-PO_4) mechanically preloaded with iron chloride and urea in the lumen 2) in the second

the synthesis is preceded by a further pre-functionalization step of the iron salt with clove essential oil (EO) as a green functionalization agent. Structural, morphological, textural, and magnetic properties were assessed by TEM, N_2 physisorption, TG-FTIR, ICP, XRD, magnetic and magnetic hyperthermia measurements. The MW-assisted solvothermal deposition of IONs was fully controlled using the phosphorylated nanoreactor, in short synthesis times, by a simple methodology following the principles of sustainable chemistry. IONs were selectively deposited on the outer surface or in the inner lumen of HNTs yielding easily recoverable superparamagnetic and thermally responsive nanocarriers suitable for applications like targeted hyperthermia therapy.

Keywords: halloysite nanotubes, magnetic nanocomposites, Microwaves, selective functionalization, iron oxide nanoparticles

1. Introduction

Halloysite is a naturally-occurring aluminosilicate with an ordered nanostructure and a characteristic hollow tubular configuration which has been widely investigated over the few last years [1,2]. Halloysite nanotubes (HNTs) have a peculiar set of physicochemical properties such as biocompatibility [3], thermal stability [4], and defined morphology [5]. In addition, given their low cost, widespread availability, and the possibility of easily tuning their surface while preserving their tubular structure, they represent a very promising class of materials for various applications [6–12].

The lumen of HNTs is an empty confined space which can be loaded and used as a carrier for the transport of many different active chemical substances, such as antibacterial agents [13–15], drugs (particularly chemotherapeutic compounds) [16–18], flame retardants [19], anticorrosive coating in ion batteries [20], catalysts [21–23], quantum dots [24,25], and metal oxide[10] and metal nanoparticles [26,27].

Being able to drive HNTs toward specific sites and activate them by external stimuli can strongly enhance their performance. Advanced approaches have been recently proposed to produce bifunctional HNTs capable both of carrying and delivering active

substances, or catalysts, and reacting to external magnetic fields [16,19,28]. These HNTs can thus be more easily driven to and activated in target sites. They also allow cheaper separation, recovery, and reuse. In fact, bifunctional HNTs endowed with magnetic properties can be mechanically manipulated and recovered by a magnet.

The classical approach to providing non-magnetic materials with magnetic properties is to produce a composite [29]. Materials are usually grafted with iron oxide nanoparticles (IONs), such as magnetite and maghemite, due to their excellent magnetic properties [30,31]. HNTs with magnetic properties have been synthesized and there are several examples of applications [32,33,42–51,34,52–57,35–41]. The location and distribution of the magnetic nanoparticles depend on the approach used for the synthesis and they also condition the final application. For instance, when HNTs are designed as carriers (drug delivery or active agents), the best approach is to functionalize the external surface while the empty lumen remains available to load the active phase. Conversely, in applications such as catalysis, the inner surface should be functionalized to leave the external area available to anchor the active catalytic sites.

The selective functionalization of the inner or outer surfaces of the halloysite nanotube can be challenging.

The external surface of HNTs, in fact, is made up of siloxane groups (Si-O-Si), while the inner wall hosts aluminol groups (Al-OH). This chemical arrangement results in a clay nanotube with a negatively charged external surface and a positively charged inner lumen. The in-situ co-precipitation of IONs is therefore favoured by electrostatic interaction, on the external surface (ION_{ext}-HNTs). Several authors have prepared ION_{ext}-HNT composites using different iron salt precursors ($FeSO_4$, $FeCl_2$, $FeCl_3$), hydrolyzing agents (NaOH, NH_4OH, $NaBH_4$), and reaction conditions [32–55].

On the other hand, the synthesis of IONs within the HNTs' hollow lumen (ION_{int}-HNTs) is less advanced and few results are available in the literature. The diffusion of cations (Fe^{3+}/Fe^{2+}) into the positively charged inner lumen is difficult or not feasible, thus restricting the use of cheap iron salt precursors to produce magnetite/maghemite phases. Zheng et al. [32] functionalized the positively charged HNT lumen by pre-loading negatively-charged urease. Hydrolysis of urea was then catalyzed by urease and the alkaline environment promoted by the reaction led to the co-precipitation of Fe^{3+}/Fe^{2+} mainly in the confined tubular HNT lumen.

However, this innovative synthesis makes use of an expensive biocatalyst (urease), which works only under restricted soft reaction conditions, leading to an increase in the overall production cost of the magnetic composite. In a different approach, the thermal decomposition of a $Mn^{2+}Fe^{3+}$–oleate complex was reported [34]. This precursor can act as both a ferrite precursor and an HNT lumen modifier, resulting in an inner ION_{int}-HNT composite material. However, the process was carried out at a high temperature (420 °C) and for a long reaction time (120 min). Strategies to ensure, by simple procedures, the selective functionalization of the inner/outer HNT surfaces with magnetic nanoparticles are therefore needed.

This paper presents a novel approach to synthesizing IONs in the selectively modified lumen (ION_{int}-HNTs) or in the external surface (ION_{ext}-HNTs) of HNTs. By following different methodologies, which include a green synthesis approach, we established different experimental protocols in order to obtain a family of easily-recoverable magnetic composite materials that can be used as carriers (ION_{ext}-HNTs) for the controlled release of active agents, or as catalytic supports (ION_{int}-HNTs).

The synthesis of ION-HNT composites was performed by in-situ homogeneous precipitation, using two different iron precursors ($FeCl_2.4H_2O$ and Fe^{2+}-$Eugenol_{complex}$), urea as the hydrolysis agent, and phosphate modified clay nanotubes as confined reactors [58], with nanoscale lumen dimensions, to promote urea hydrolysis. A microwave (MW) assisted process was carried out using a homemade high-pressure stainless-steel reactor [59]. The reactor configuration enables the MW energy to be applied directly inside the reaction medium, using a coaxial antenna[60,61]. This method has already been successfully used to synthesize a wide gamma of different materials like superparamagnetic IONs [31], silver nanoparticles[62], dye-doped polymeric microresonators[63] and mesoporous ordered silica-based frameworks [64]. In the MW solvothermal synthesis, mild conditions (temperature and pressure) are used to enhance the overall desired reactions. According to the reports, urea hydrolysis and the homogeneous precipitation of IONs nanoparticles are favoured by these conditions, and a higher crystallinity of the IONs is also promoted [65].

The textural, structural, morphological, and magnetic properties of this novel family of magnetic (ION_{int}-HNTs and ION_{ext}-HNTs) nanomaterials were assessed by several

techniques (multinuclear MAS NMR, FTIR, TGA, TEM, N_2 physisorption and magnetometry) and are discussed.

2. Experimental section

2.1 Materials

Pristine halloysite nanotubes (HNTs), sulfuric acid (H_2SO_4, 98%) and phosphoric acid (H_3PO_4, 85%) were purchased from Sigma-Aldrich and used without further purification. Iron(II) chloride tetra-hydrate ($FeCl_2.4H_2O$, 99%) and urea (NH_2CONH_2, 99%) purchased from Sigma-Aldrich were used as the iron precursor salt and as the hydrolyzing agent, respectively. Deionized water obtained with a Milli-Q system (Millipore, Bedford, MA, USA) and ethylene glycol purchased from Fluka Analytical (99.9%) were used as solvents for ION-HNTs synthesis in the MW-assisted hydrothermal route.

2.2 HNT acid etching and phosphate functionalization

HNTs were initially modified by lumen etching leading to acid etched HNTs-(H^+) following a procedure already described [13]. The phosphoric acid reaction with HNTs-(H^+) was then performed as described elsewhere [58]. Briefly, HNTs-(H^+) were dispersed into H_3PO_4 saturated aqueous solution. The suspensions were evacuated in a vacuum jar, for 3 h, and then cycled back to atmospheric pressure. This process was repeated three times to increase the loading efficiency. Finally, HNTs were separated from the solution by centrifugation, washed with water and dried in an oven at 70 °C. A thermal treatment was then performed at 320 °C for 2 h under static air conditions to produce HNTs-(H^+-PO_4).

2.3 *Preparation of HNT-ION composites: MW-assisted hydrothermal approach*

The magnetic composite materials were obtained using a 250 ml homemade stainless steel pressurized reactor, equipped with a coaxial antenna as a microwave applicator.

It has recently been shown that this configuration allows the synthesis of ION nanoparticles with magnetic properties in a very short reaction time [31]. The MW-assisted hydrothermal reactor is described in detail elsewhere [31,59,64]. The MW source is a commercial magnetron oscillator equipped with forward and reflected power indicators (SAIREM, Mod. GMP 03 K/SM, supplying up to 300 W of continuous MW irradiation power at a frequency of 2.45 GHz). A satisfactory MW impedance matching between the reactor and the MW source was obtained by configuring the active section of the applicator as a function of the permittivity of the reagents (ethylene glycol-water mixtures showed a strong MW absorption affinity). In addition, the presence of iron ions during the first step and the high MW absorption of magnetic nanoparticles produced, matched well with the proposed MW process. Three different composite materials were prepared starting with HNTs-(H^+-PO_4).

ION_{ext}-HNTs-1 were obtained by direct solvothermal deposition of IONs on the external surface of HNTs-(H^+-PO_4). Firstly, urea was loaded in the hollow HNTs-(H^+-PO_4) lumen by a mechanical process. Briefly, 5 g of HNTs-(H^+-PO_4) were added to 30 mL of ethanol and dispersed for 5 min using ultrasound. A total of 1.5 g of urea dissolved in 10 mL of ethanolic aqueous solution (40% vol) was then added to HNTs-(H^+-PO_4) dispersion. The suspension was evacuated in a vacuum jar for 30 min, and then cycled back to atmospheric pressure. This process was repeated three times in order to increase the urea loading efficiency (vacuum driven lumen filling of HNT has been proved as highly efficient approach[66]). HNTs-(H^+-PO_4)-urea were then separated from the ethanol-water mixture by solvent evaporation in an oven. A total 3 g of $FeCl_2.4H_2O$ and the HNTs-(H^+-PO_4)-urea were added to 50 mL of ethylene glycol-water mixture (volume ratio 1.5:1) used as a reaction solvent system. The mixture was stirred for 5 min and then loaded onto the stainless-steel reactor equipped with a Teflon vessel, and the reactor was closed. An initial pressure of 6 bar was adjusted with N_2 gas. The reaction temperature was set to 175 °C reached in 5 min by applying 200 W of

MW power. The reaction was then carried out for 30 min using 50 W of MW. Due to the urea hydrolysis, the reaction pressure was increased up to 8 bar at 175 °C (working temperature). After 30 min of MW irradiation, the power supply was switched off and the reactor was allowed to cool naturally to complete the reaction. The pressure was released to atmospheric conditions and the ION_{ext}-HNTs-1 were centrifuged, washed with ethanol-water several times, and dried at 70 °C overnight.

ION_{int}-HNTs-2 were similarly obtained by solvothermal deposition of IONs but on the internal surface of HNTs-(H^+-PO_4). In this case clove EO was used to produce a different iron precursor (always starting from $FeCl_2.4H_2O$). Clove EO with a high eugenol composition (> 70%) was obtained by a MW-assisted hydrodistillation procedure reported elsewhere [67,68]. A total of 3 g of $FeCl_2.4H_2O$ were dissolved in 10 ml of ethanol and 5 g of clove EO were added dropwise to this solution. The solution was stirred for 30 min while the color changed from colorless to dark blue, indicating a fast reaction of iron ions with eugenol $(Fe^{2+}\text{-Eugenol})_{complex}$. A second solution was prepared as follows: 5 g of HNTs-(H^+-PO_4) were added to 30 mL of ethanol and dispersed for 5 min using ultrasounds. A total of 1.5 g of urea dissolved in 10 mL of ethanolic aqueous solution (40% vol.) was then added to HNT-(H^+-PO_4) dispersion. The iron precursor $(Fe^{2+}\text{-Eugenol})_{complex}$ and HNTs-(H^+-PO_4)-urea suspensions were then mixed, evacuated in a vacuum jar, for 30 min, and then cycled back to atmospheric pressure. This process was repeated three times to increase the loading efficiency. $(Fe^{2+}\text{-Eugenol})_{complex}$-HNTs-($H^+$-$PO_4$)-urea were then separated from the suspension by solvent evaporation in an oven. The resulting solid mixture $(Fe^{2+}\text{-Eugenol})_{complex}$-HNTs-($H^+$-$PO_4$)-urea) was added to 50 mL of ethylene glycol-water mixture (volume ratio 1.5:1) used as a reaction solvent system. The mixture was stirred for 5 min and then loaded to the MW-assisted reactor and treated as ION_{ext}-HNTs-1 ($P_{0,N2}$=6 bar, T_{rxn}=175 °C t_{rxn}=30 min). After the reaction time had finished, the power supply was switched off and the reactor was allowed to cool naturally in order to complete the reaction. The pressure was released to atmospheric conditions and the ION_{int}-HNTs-2 were centrifuged, washed with ethanol-water several times, and dried at 70 °C overnight.

$ION_{int\text{-}ext}$-HNTs-3 were obtained using the same experimental approach described above for ION_{int}-HNTs-2, however several cleaning steps with hexane were performed after the vacuum loading cycles and before drying. After this, the MW-assisted process,

separation and purification were the same as ION_{int}-HNTs-2. All the synthesis protocols are illustrated in Scheme 1.

2.4 Characterization

2.4.1 Fourier-transform infrared spectroscopy

Infrared spectra were recorded using an FT-IR Agilent Technologies Spectrophotometer model Cary 640, equipped with a universal attenuated total reflectance (ATR) accessory. A few micrograms of dry and purified HNTs sample were used with the following spectrometer parameters; resolution: 4 cm^{-1}, spectral range: 600–4000 cm^{-1}, number of scans: 16. Agilent spectrum software was used to process FTIR spectra.

2.4.2 Nitrogen physisorption

Nitrogen adsorption and desorption isotherms were recorded at 77 K using a Beckman Coulter SA 3100 surface area analyser. All the samples were outgassed for 120 min at 50 °C under vacuum conditions ($P=10^{-3}$ mmHg). The isotherm was measured over the relative pressure range (P_S/P_0) from 0.01 to 0.991. The specific surface area (S_{BET}) was calculated using the Brunauer-Emmett-Teller (BET) equation in the low relative pressure interval from 0.05 to 0.2. The Langmuir model and the t-plot method were used to obtain further information on the size of the monolayer and micropore volume at lower relative pressures ($P_S/P_0<0.05$). Total pore volume was determined at the relative adsorption pressure of 0.9814. The pore size distribution was calculated with the adsorption branch of the isotherm using the Barrett-Joyner-Halenda (BJH) method.

2.4.3 Thermogravimetry

A TA Instruments Thermobalance model Q5000IR equipped with an FTIR (Agilent Technologies) spectrophotometer Cary 640 model for evolved gas analysis (EGA) was used. TG measurements were performed at a rate of 10 °C/min, from 25 °C to 800 °C under nitrogen flow (25 mL/min) using Pt crucibles. TG-FTIR measurements were performed at a rate of 20 °C/min, from 30 °C to 900 °C under nitrogen flow (70 mL/min), from 500 to 3000 cm^{-1} with a 4 cm^{-1} width slit. A background spectrum was taken before each analysis in order to zero the signal in the gas cell and to eliminate the contribution due to the amount of ambient water and carbon dioxide. The amount of sample in each experiment varied between 4 and 8 mg. Mass calibration was performed using certified mass standards, in the range from 0 to 100 mg, supplied by TA Instruments. Temperature calibration was based on the Curie point of paramagnetic metals. A multipoint calibration with five Curie points from reference materials (Alumel, Ni, Ni83%Co17%, Ni63%Co37%, Ni37%Co63%) was performed[69].

2.4.4 Transmission electron microscopy

ION-HNT composites were examined by transmission electron microscopy (TEM). The powders were suspended in 2 mL of isopropanol, and a few drops of the suspensions were deposited onto copper grids. The solvent was then left to evaporate at room temperature. Images were acquired using a CM12 Philips transmission electron microscope equipped with a microanalysis Edax and LaB6 cathode.

2.4.5 Induced Coupled Plasma – Atomic Emission Spectroscopy

Elemental analysis was carried out with a Varian 720-ES inductively coupled plasma-atomic emission spectrometer (ICP-AES). For the analysis, approximately 1 mg of sample was digested by concentrated aqua regia (HCl suprapure and HNO_3 subboiled in a 3:1 ratio) with a few drops of HF. Calibration standards were prepared by gravimetric serial dilution from the standard at 1000 mg/L. The wavelengths used for Al, Fe and Si were 369.152, 238.204 and 251.432 nm, respectively.

2.4.6 *Magnetic Measurements*

The magnetic behaviour of ION-HNT composites was evaluated using a vibrating sample magnetometer (VSM, Quantum Design PPMS). The powder samples were hosted in Teflon tape and the obtained magnetization values were normalized by the iron percentage in the sample obtained from ICP-AES measurements. Zero-field-cooled/field-cooled (ZFC/FC) curves were obtained by measuring the temperature dependence of the magnetization by applying a probe magnetic field (5 mT) after cooling the sample in the absence (ZFC) or in the presence (FC) of the field. The saturation magnetization (Ms) of the ION-HNT composites was estimated from the magnetization curves, extrapolating high field data with the empirical law (eqn. (1)):

$$M = M_S + \frac{a}{H} + \frac{b}{H^2}, \text{----------(1)}$$

where H is the external magnetic field.

2.4.7 *Magnetic Hyperthermia Measurements*

Magnetic hyperthermia experiments were carried out on an experimental setup based on a 6 kW Fives Celes power supply operating at a frequency of 183 kHz and a field amplitude of 17 kA/m (213 Oe). The samples were placed in a polystyrene sample holder and introduced inside a glass tube thermostated at 25°C using an ethylene glycol flow. The temperature was recorded by an optical fibre in contact with the sample. The measurements were collected in triplicate, and the specific absorption rate (SAR) was determined according to eqn (2):

$$SAR = \frac{\sum_i m_i c_{pi}}{m_{Me}} \Delta T / \Delta t \text{--------(2)}$$

where the sum is extended to all the i species involved in the heat exchange (here HNT and ION), mi is the mass in g of the i-species and Cpi their specific heat. Since the measurement setup was non-adiabatic, $\Delta T/\Delta t$ was extrapolated from the initial slope of the calorimetric curve.

3. Results and discussion

3.1 MW-assisted hydrothermal cascade reactions for in situ ION synthesis on phosphate-modified HNTs: general approaches

The synthesis of magnetic ION-HNT composites was performed in several steps. The general synthesis protocol is illustrated in Scheme 1 and fully described in the experimental section.

Confined nanoreactors with phosphorylated catalytic sites, HNTs-(H^+-PO_4), (step 1 in scheme 1) were prepared and fully characterized as described in ref. [58]. In fact, phosphoric acid has been reported as an efficient polyprotic acid that significantly enhances the urea hydrolysis rate [70].

The homogeneous precipitation of iron-oxide nanoparticles was performed following two different approaches to obtain magnetic composites by the solvothermal deposition on the external surface (ION_{ext}-HNTs) or in the inner HNT lumen (ION_{int}-HNTs).

The first approach (black round-dot line arrow in Scheme 1) was performed by directly loading, into the MW-assisted reactor, the solvent (ethylene glycol-water mixture) together with HNTs-(H^+-PO_4) previously mechanically loaded with iron chloride and urea precursors in the lumen. The confinement of phosphate groups in HNTs-(H^+-PO_4), promotes a rapid urea hydrolysis both in the inner lumen and in the surrounding environment due to both: i) the catalytic reaction with the hydrogen phosphate active sites anchored to the nanotube mesopores, and ii) urea thermolysis at 175 °C during MW heating. The consequent formation of OH^- anions increases the pH, thus fostering the in-situ precipitation of iron-oxide nanoparticles in the alkaline reaction medium. Following this approach, we obtained magnetic (ION_{ext}-HNTs-1) composites.

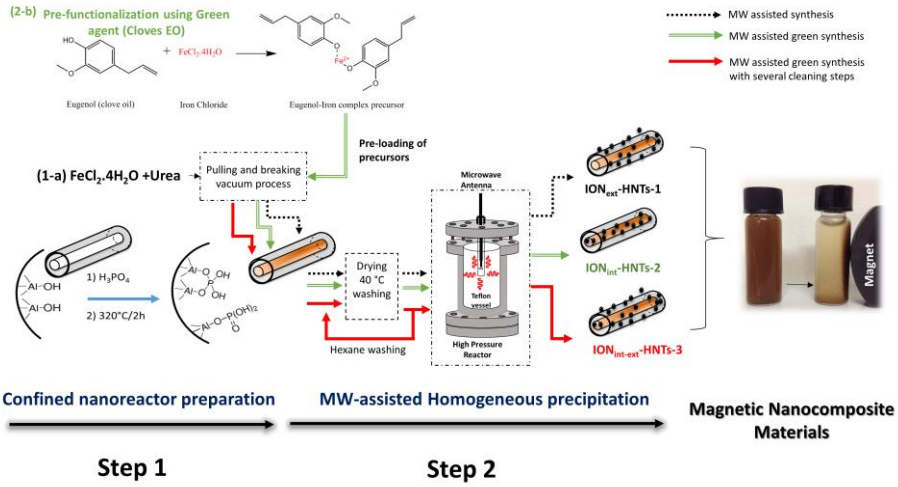

Scheme 1. General experimental approaches to synthesize magnetic composite: IONs deposited onto the external surface (ION_{ext}-HNTs-1), internal surface (ION_{int}-HNTs-2) and internal-external surface ($ION_{int\text{-}ext}$-HNTs-3) area of HNTs.

A second synthetic green approach (green double-line arrow in Scheme 1) was also developed to obtain the ION_{int}-HNTs through a different loading protocol. The synthesis was carried out following the same experimental procedure used for ION_{ext}-HNT-1 composites, preceded by a further pre-functionalization step of the iron salt precursor with clove essential oil (EO) as a green functionalization agent (see reaction 2-b in Scheme 1).

We have previously reported the successful use of EO to synthesize metal nanoparticles in a fast MW-assisted reaction [62]. In fact, EO acts as a renewable reducing agent, avoiding the need for surfactants or other chemical compounds.

Moreover, pre-functionalizing the iron salt allows to exploit the different solubilities of the various precursors in an appropriate solvent. Hexane completely dissolves the eugenol/iron complex, while urea remains insoluble. Cleaning with hexane promotes the selective removal of the iron complex from the solution and, due to its strong hydrophilic character, also from the external surface of the HNTs. This approach enables a high loading of iron-urea precursors in the lumen of HNTs preventing the formation of IONs on the external surface. The MW-assisted process then yields the

330 ION_{int}-HNT-2 composite material. It has also been shown that the use of eugenol does not affect the ION formation [71].

Surprisingly, we observed that by increasing the cleaning steps with hexane before the MW-assisted homogeneous precipitation (red solid-line arrow in Scheme 1), stable magnetic nanocomposite with IONs localized in both internal and external HNT 335 surfaces were produced, yielding an $ION_{int-ext}$-HNT-3 nanocomposite material. This result is not easy to explain but it could be due to the partial removal of the iron complex from the lumen of the nanotube, which creates favourable conditions for the synthesis of IONs on both surfaces of the nanotube.

Table 1 enlists the textural properties of the phosphorylated nanotubes and of the 340 derived magnetic nanocomposites ION_{ext}-HNT-1, ION_{int}-HNT-2, and $ION_{int-ext}$-HNT-3. The textural properties of the HNTs-(H^+-PO_4) changed depending on the location of IONs. BET surface area, pore volume and monolayer volume decrease when IONs are synthesized in the hollow lumen (see Table 1). BET surface area of ION_{ext}-HNT-1was higher than the starting HNTs-(H^+-PO_4) probably because the contribution of IONs 345 surface area deposited on the external surface of HNTs.

Table 2 shows the reaction conditions used in this work to prepare three different magnetic ION-HNT composites and compares them with various approaches reported in the literature. The saturation magnetization (Ms) of the ION-HNT composites is also compared.

350 **Table 1.** Textural properties of modified HNTs with phosphoric acid and IONs.

Sample	lumen modification	Textural properties		
		[1]BET Area, m^2/g	[2]Pore volume (Ads) cm^3/g	Monolayer volume, cm^3/g
HNTs- (H^+-PO_4)	Modified with H_3PO_4	98	0.25	22.52
ION_{ext}-HNTs-1	IONs external surface area	124	0.25	28.51
ION_{int}-HNTs-2	IONs mainly in the internal lumen	66	0.19	15.13
$ION_{int-ext}$-HNTs-3	IONs in both internal and external surface areas	72	0.20	16.59

[1]Calculated with the Brunauer Emmet Teller equation in the linear interval of relative pressure from 0.05 to 0.2

[2]Total Pore volume, calculated at the relative pressure of 0.9814

The comparison clearly shows that the methodologies developed here allow to obtain magnetic nanocomposites in short reaction times (due to the use of MWs)

with a good control of the localization of the IONs (on the HNT external surface or in the lumen), and with high values of Ms. It is worthy to point it out that ION_{int}-HNTs-2 have the highest magnetic properties (Ms=31 emu/g) among of the corresponding HNT having IONs localized in the hollow lumen (i.e Ms=2.8[45,46], 4.2[37], 5.7[32], 8.5[38] and 11.5[51] emu/g). $ION_{int-ext}$-HNTs-3 also have higher magnetization (Ms=33 emu/g) than the reported HNT having IONs localized in the internal/external surface (Ms≈25 emu/g)[28]. The magnetic properties of ION_{ext}-HNTs-1 (Ms=27 emu/g) are in line with the corresponding HNT with IONs localized in the external surface which Ms ranges from 1.2 to 42.7 (Table 2). Furthermore, the comparison of Fe_3O_4-HNTs having the highest magnetic properties (Ms=42.7 emu/g, synthesis conditions: T=200 °C, t=8 h) [55], highlights the MW-assisted solvothermal method here reported as an appealing reaction system in terms of both Ms obtained in short extraction times (30 min at 175°C) and for its innovative use of an alternative energy sources.

A full characterization of these materials is presented and discussed below.

Table 2. Different approaches to synthesize ION/HNT composite materials reported in the literature and in this work. Reaction conditions and the saturation magnetization are also listed.

Composite	IONs on the HNTs	Heating approach	Iron precursor	Hydrolyzing agent	Reducing agent	time (min)	T (°C)	Ms (emu/g) T=300K	Ref.
ION_{ext}-HNTs-1	external surface	MW	$FeCl_2$	Urea /HNTs-(H^+-PO_4)		30	175	27	This work
ION_{int}-HNTs-2	hollow lumen		$FeCl_2$-Clove EO complex					31	
$ION_{int-ext}$-HNTs-3	internal/external surface							33	
Fe_3O_4-HNTs	hollow lumen	CH	$FeSO_4/FeCl_3$	urea	urease	30	65	5.7	[32]
Fe_3O_4-HNTs	external surface	CH	$FeSO_4/FeCl_3$	NH_3H_2O solution		240	70	27.9	[33]
Fe_3O_4-HNTs	external surface	CH	$FeSO_4/FeCl_3$	NH_3H_2O solution		90	70	25.4	[34]
Fe_3O_4-HNTs	external surface	--------	$FeCl_3$	$NaBH_4$		30	RT	N.R.	[35]
Fe_3O_4/C-HNTs		CH		$NaBH_4$/glucose		720	180	1.9	
Au/HNTs/Fe_3O_4	external surface	CH	$FeCl_2/FeCl_3$	NH_3H_2O solution/L-lysine		60	70	24.1	[36]
$MnFe_2O_4$/HNTs	hollow lumen	CH	$Mn^{2+}Fe^{3+}$–oleate complex	Thermal decomposition		120	450	4.2	[37]
	external surface		$Mn^{2+}Fe^{3+}$–oleate complex/water					1.9	
Fe_3O_4-HNTs	hollow lumen	CH	$FeCl_2/FeCl_3$	NaOH		150	50	8.5	[38]
Fe_3O_4-HNTs	internal/external surface	CH	$FeSO_4.7H_2O$/ $FeCl_3.6H_2O$	NH_4OH		240	80	≈25*	[28]

N-doped GQDs/ Fe_3O_4-HNTS	external surface	CH	$FeSO_4.7H_2O$/ $FeCl_3.6H_2O$	NH_4OH	360	70	N.R.	[39]
Fe_3O_4-HNTs-CS	external surface	CH	$FeCl_3.6H_2O$-Na_2SO_3	NaOH	30	100	18.4-20	[40,41]
Co-HNTs	external surface	CH	$CoSO_4$, $NaPO_2H_2$, NH_4Cl, and sodium citrate	Na_2PdCl_4-PVP (electroless deposition)	N.R.	80	37.9	[42]
Fe_3O_4-HNTs	external surface	CH	$FeSO_4.7H_2O$/ $FeCl_3.6H_2O$	NH_4OH	300	70	N.R.	[43]
Fe_3O_4-HNTs	external surface	--------	$FeCl_2$/$FeCl_3$	NaCl/KOH (mechanochemical synthesis)	30	RT	1.2	[44]
Fe_3O_4-HNTs	hollow lumen	CH	$Fe(NO_3)_3{\cdot}9H_2O$	Ethylene glycol/heating treatment	20 h	400	2.8	[45,46]
Fe_3O_4–MnO_2-HNTs	external surface	CH	$FeSO_4.7H_2O$/ $FeCl_3.6H_2O$	NH_4OH	240	70	27.8	[47]
Fe_3O_4-HNT	external surface	CH	$FeSO_4.7H_2O$/ $FeCl_3.6H_2O$	NH_4OH	135	80	N.R.	[48]
Fe_3O_4-HNTs	external surface	CH	$FeSO_4.7H_2O$/ $FeCl_3.6H_2O$	NH_4OH	360	RT	35.9	[49]
Fe_3O_4-HNTs	external surface	CH	$FeSO_4.7H_2O$/ $FeCl_3.6H_2O$	NaOH	180	70	≈10	[50]
Fe_3O_4-HNTs	hollow lumen	CH	$FeSO_4.7H_2O$/ $FeCl_3.6H_2O$	NH_3-H_2O solution	300	70	11.5	[51]

Fe_3O_4-HNTs	external surface	CH	$Fe(NO_3)_3 \cdot 9H_2O$	Acetic acid/heating treatment	200	60	N.R.	[52]
Fe_3O_4-HNTs	external surface	CH	$FeSO_4.7H_2O$/ $FeCl_3.6H_2O$	NH_4OH	240	70	27.8	[53]
Fe_3O_4-HNTs-Ag	external surface	CH	$FeSO_4.7H_2O$/ $FeCl_3.6H_2O$	NH_4OH	180	60	6.1	[54]
Fe_3O_4-HNTs	external surface	-------	$FeCl_3.6H_2O$	$NaBH_4$	30	RT	1.9	[35]
Fe_3O_4-HNTs	external surface	CH	$FeCl_3.6H_2O$	CH_3COONa	8 h	200	42.7	[55]
Mag-HNTs	internal/external surface	CH	$FeCl_2/FeCl_3$	NaOH	30	75	----	[57]

The morphology, particle size and location of IONs loaded on the HNTs-(H^+-PO_4) surface were examined by transmission electron microscopy (TEM). Figure 1(a) shows a pristine HNT sample with a well-defined tubular shape, open-ended empty lumen with 50 nm outer diameter, 250 nm length and, between 15 to 20 nm inner diameter. After modification and ION loading, all ION-HNTs maintain their cylindrical shape. ION_{ext}-HNTs-1 (obtained by direct precipitation) are fully covered with IONs (average particle size of 2-3 nm) located on the external surface (see Fig.1(b, b1) and Fig.S1(a, a1). The ION particles have mainly a spherical morphology and are extensively aggregated. Some rod-like morphology is also observed in Figs. 1(a) and S1(a)

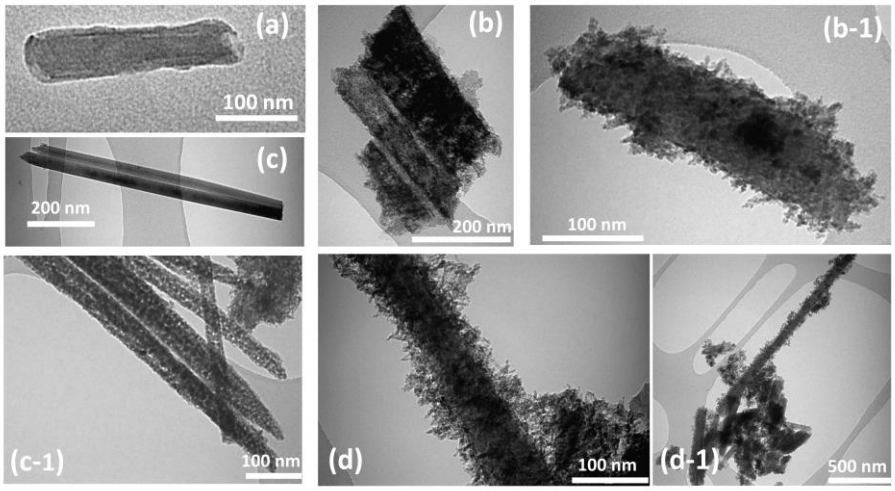

Figure 1. TEM images (at different magnifications) of pristine HNTs (a), ION_{ext}-HNTs-1 (b, b-1), ION_{int}-HNTs-2 (c, c-1) and $ION_{int\text{-}ext}$-HNTs-3 (d, d-1) magnetic composite materials.

In $ION_{int\text{-}ext}$-HNTs-3 both internal and external surfaces of (fig. 1(d) and fig. S1(b)) are covered with spherical ION particles, however there are also some rod-like nanoparticles on the outer surface. The spherical nanoparticles show the same aggregation pattern as in ION_{ext}-HNTs-1 with individual particle sizes of around 3-4 nm.

On the other hand, ION_{int}-HNTs-2 exhibit a very smooth external surface (see fig. 1(c, c-1)) while the lumen shows an irregular filling along the nanotube (free sections from 4 nm to fully obstructed, fig. S1(c)).

Elemental analysis (ICP-AES) indicated the effective presence of iron in all the ION-HNT composites, with a weight percentage of 5.1, 7.8 and 6.6% for ION_{ext}-HNTs-1, ION_{int}-HNTs-2 and $ION_{int-ext}$-HNTs-3, respectively (Table 3). The X-ray powder diffraction analysis of the ION-HNT composites (data not shown) did not provide a clear detection of iron oxide nanostructures over the HNTs. In fact, the partial superimposition of the diffraction pattern of magnetic iron oxides (magnetite, maghemite) and that of halloysite prevented a clear identification of the phase of the IONs, in particular the broadening of the diffraction peaks characteristic of nanosized materials.

Figure 2 shows the adsorption and desorption nitrogen isotherms of ION_{ext}-HNTs-1, ION_{Int}-HNTs-2 and $ION_{Int-ext}$-HNTs-3and the BET surface area and pore dimensions are listed in Table 1. For iron oxide nanoparticles selectively loaded outside the HNT structure (ION_{ext}-HNTs-1), the surface area (124 m^2/g) and monolayer capacity (monolayer volume=28.51 cm^3/g) were found to be higher than that of the phosphorylated parent HNTs-(H^+-PO_4) (surface area=98 m^2/g, monolayer volume=28.51 cm^3/g), while the total pore volume was unchanged (0.25 cm^3/g). The higher surface value found is consistent with the presence of ION nanoparticles on the external surface. On the other hand, halloysite nanotubes with IONs loaded within the hollow (ION_{Int}-HNTs-2 and $ION_{ext-int}$-HNTs-3), showed a pronounced reduction in the surface area (from 98 to 66 and 72 m^2/g, respectively) and pore volume (from 0.25 to 0.19 and 0.20 cm^3/g, respectively), which was still more evident for ION_{Int}-HNTs-2 (see full data listed in Table 1). Concerning the isotherm form, all three nanocomposites show a characteristic type IV-a isotherm with an H-3 hysteresis loop (see Fig. 2-a), The hysteresis loop of ION_{ext}-HNTs-1 has the same width as that of the parent material, confirming that no IONs were formed inside the halloysite nanotubes. For nanocomposites with IONs loaded within the lumen (ION_{Int}-HNTs-2 and $ION_{Int-ext}$-HNTs-3), the hysteresis loop is narrower, suggesting the formation of iron oxide nanoparticles in the phosphate active sites. Although no exact conclusions can be drawn regarding the particle size, the IONs did not result in pore blocking or saturation.

Figure 2-b shows the pore size distribution functions for all three materials. There is a broad pore distribution with no significant peaks above 12 nm in average diameter.

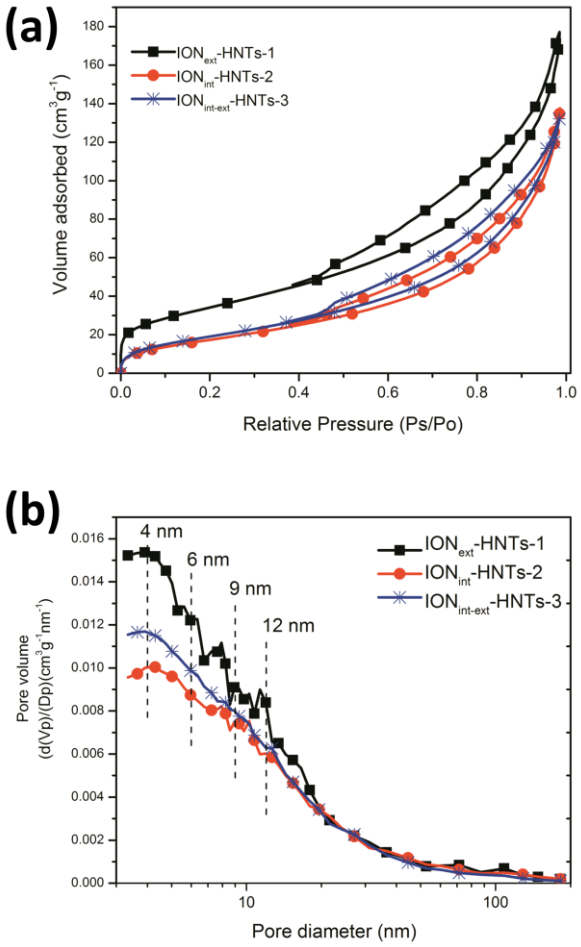

Figure 2. N_2 adsorption/desorption isotherms (a) and pore size distribution (b) of ION-HNT magnetic mesoporous composites.

Figure 3 shows the TG (a) and DTG (b) curves for ION-HNT composites. ION_{ext}-HNTs-1 show similar thermal properties to that of the parent material HNTs-(H^+-PO_4) [58], with two main mass losses at 32 °C and at 449 °C related to the loss of adsorbed and chemically bound water, respectively. The IONs deposited on the external surface

do not modify the thermal profile of HNTs, since they were very stable under nitrogen throughout the temperature range of the experiment [31].

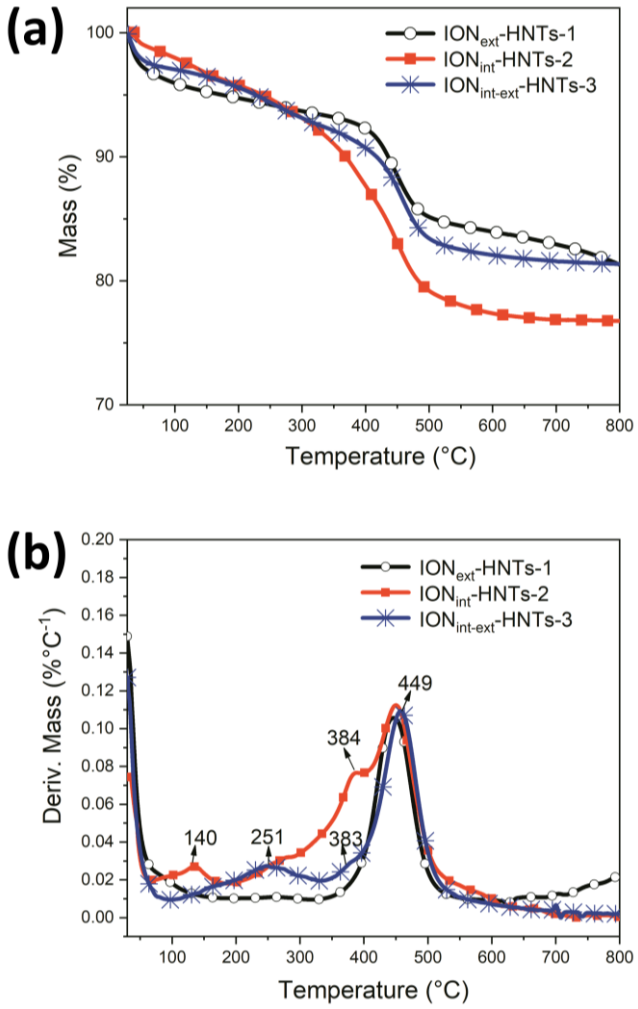

Figure 3. Thermogravimetric curves (a) and their derivatives (b) of ION-HNT composites performed under nitrogen flow at 10°C/min heating rate

The TG curves of the ION$_{Int}$-HNTs-2 and ION$_{Int-ext}$-HNTs-3 samples, obtained using Fe^{2+}-Eugenol$_{complex}$ as an iron precursor, have a more complex thermal profile with further mass losses in the range 140-385 °C. The FTIR analysis of the evolved gases highlighted that these mass losses are due to the degradation of adsorbed eugenol (fig.

S2). In fact, the FTIR spectrum, reveals signals related to the degradation of the methoxy moiety (at about 2190 and 2100 cm^{-1}, CO stretching) and to the volatilization of the phenolic residue (at 3650 cm^{-1} and 1288 cm^{-1}, OH stretching and bending, at 3053 cm^{-1}, C-H stretching, at 1595 and 1500 cm^{-1}, C=C stretching at 1185 cm^{-1} C-O stretching, and at 878, 757 and 696 cm^{-1} C-H bending) of eugenol.

The mass loss at 140 °C of ION_{int}-HNTs-2 is likely due to the loss of eugenol adsorbed on the external wall of the HNTs, while the mass losses at higher temperatures of both ION_{Int}-HNTs-2 and $ION_{Int-ext}$-HNT-3 are probably related to eugenol absorbed to IONs located on the external wall (mass loss at 251 °C) or in the inner HNT lumen (383-384 °C), respectively.

The magnetic properties of the ION-HNT composites were investigated as a function of both temperature and magnetic field. Figure 4a) reports the magnetization curves as a function of the temperature after zero field cooling (ZFC) and field cooling with a magnetic field of 50 Oe (FC). All the composites show the typical thermal irreversibility of nanosized magnetic materials, but the curves present no clear features. The ZFC curves are characterized by the presence of a broad maximum, likely due to the size and shape dispersions and, above all, to the strong interparticle interactions. TEM analysis, in fact, shows that the individual particles are arranged in large aggregates onto the surfaces (internal and external) of the halloysite structure.

It is worth underlining that at low temperatures, all the ZFC curves increase monotonously, indicating the absence of paramagnetic phases in the composites, such as unreacted Fe(II). Moreover, no evidence of magnetic order transition can be observed in either the ZFC and FC curves.

Table 3. Iron weight percentage and magnetic properties of ION-HNT composites.

Sample	Fe% w/w	M5T		MS		Hc (Oe)
		10 K	300K	10K	300K	10K
ION_{ext}-HNTs- 1	5.03	50	20	82	27	280
ION_{int}-HNTs-2	7.83	51	23	79	31	157
$ION_{int-ext}$-HNTs-3	6.61	56	26	83	33	154

The magnetization was also investigated as a function of the magnetic field, both at 10 and 300 K (Figures 4b and 4c). Saturation was not reached for any of the composites, even at the highest fields (5 T). This is likely due to the presence of antiferromagnetic phases and/or to the very small size of the IONs. In fact, the quasi-linear approach to saturation can arise from the progressive canting of the coupled spins in the first case, or from the disordered superficial spins in the second. The absence of any Nèel transition signature, however, suggests a very poor iron oxide antiferromagnetic content, if any. On the other hand, the large surface-to-volume ratio of 2-3 nm nanoparticles, and thus the large surface contribution to the total magnetization, could explain the observed behaviour.

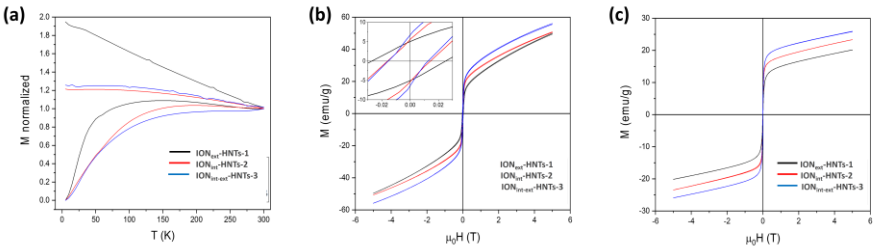

Figure 4: a) ZFC-FC magnetization of the ION-HNT composites. Data were normalized to the value of ZFC curve at 300 K. b) Magnetization curves of the ION-HNT composites recorded at 10 K. In the inset, the magnification of the low field region is reported. c) Magnetization curves of the ION-HNT composites recorded at 300 K.

The saturation magnetization (Ms) values of the ION-HNT composites obtained for the room temperature curves are in good agreement with the values in the literature for similar systems [33,34,36], although much lower than the bulk values of iron oxides with the best magnetic properties, i.e., magnetite or maghemite (90 emu/g and 80 emu/g at room temperature, respectively). Nevertheless, a decrease in Ms is commonly reported in nanosized particles and, again, is ascribed to the surface spins which are not aligned to bulk ones. The surface disorder is also responsible for the large decrease in the Ms values at room temperature found for all the samples. All the composites showed superparamagnetic behaviour at room temperature (i.e. no remanence or coercivity). On the other hand, at 10 K a hysteretic behaviour was observed, with coercive fields in the order of a few tens of mT, which is compatible with the very small size of the IONs present in the composites. From the analysis of the magnetic results, the nanoparticle structure is compatible with the iron oxide spinel phase, excluding the

antiferromagnetic phases. Two phases of iron oxide (magnetite and maghemite) could form under the reaction conditions used in this work. However, the magnetic behaviour is strongly influenced by the large contribution of the surface due to the ultra-small size of the particles. The slight differences (the shape of the ZFC-FC curves and, above all, a slight increase in the coercive field), observed in the magnetic behaviour of sample ION_{ext}-HNTs-1, are due to the use of different iron precursors in the reaction mixture, which may influence the size distribution and the crysrevtallinity of the IONs obtained. The application potential of magnetic-nanoparticle-loaded HNT is not limited to the ability to mechanically control and retrieve them using magnetic field gradients. Superparamagnetic nanoparticles are well-established nanosized heat vectors that can be heated through the application of magnetic field alternating at high frequency. This outstanding feature has been studied widely for the selective ablation of cells in the therapy of tumours [72] and is a promising means to modulate chemical reactivity through temperature control at the nanoscale [73].

Indeed, the hybrid architectures presented in this work are interesting candidates for both approaches, thanks to the full control achieved in the positioning of ION around the HNT frame. We therefore evaluated the thermal response of the three HNT nanocomposites in powder form by recording their temperature kinetics in the presence of an alternating magnetic field of 17 kA/m amplitude and 183 kHz frequency (details on the experimental setup are given in the experimental section). Temperature vs time curves under the application of an alternating magnetic field were acquired for the three ION-HNT powder samples and are reported in Figure 5. The hyperthermal performance of the ION-HNT samples was then estimated by measuring the initial slope of the temperature vs time curves and calculating the specific absorption rate (SAR).

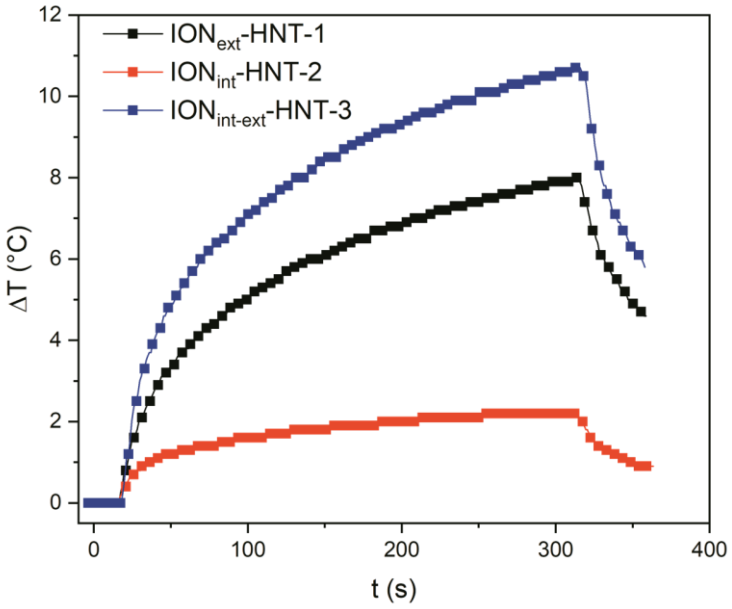

Figure 5: Temperature kinetics of ION-HNT powder samples during the application of an alternating magnetic field (17 kA/m, 183 kHz, 5 min), starting from a temperature of 25°C.

The estimated SAR values for the three samples are reported in Table 4. Even though these values are quite moderate if compared to the SAR values reported in the literature for systems proposed as hyperthermia mediators, it should be noted that the samples were not measured as a colloidal suspension, but in powder form: such difference in measuring conditions complicates the comparison with literature data. Therefore, the obtained SAR values were here reported as a rough evaluation of the bulk heating capability of ION-HNT samples. Moreover, the field parameters used in the measurements are below the physiological tolerance threshold or physiological limit [74], beyond which deleterious responses of living tissues are observed. This aspect is often overlooked in the literature, leading to high but therapeutically unserviceable SAR values. Within this framework, some of the SAR values estimated for some of the ION-HNT samples are comparable to other ION-based systems which have been

demonstrated to be effective in strongly reducing cell viability in *in vitro* hyperthermic experiments [75]. Therefore, the obtained data indicates that, despite the relatively low loading of IONs, the hybrid systems show promising potential for magnetic field-assisted hyperthermia.

Table 4. Hyperthermal performance of the three IONs-HNT systems.

Sample	SAR [W/g]
ION_{ext}-HNTs-1	2.65 ± 0.04
ION_{int}-HNTs-2	0.57 ± 0.02
$ION_{int-ext}$-HNT-3	3.28 ± 0.22

Considering that the iron loading as well as the magnetic moment at saturation are similar for the three samples, the difference in heating values reported in Table 4 can be reasonably ascribed to the topology of each sample. In particular, ION_{int}-HNTs-2 show a very low heating performance, which is compatible with the fact that iron oxide nanoparticles confined in the lumen of the HNT are separated from the external environment, therefore the heat transfer is hindered by the topology of the system. On the other hand, ION_{ext}-HNTs-1 show a heating performance that is over four times higher than ION_{int}-HNTs-2, since iron oxide nanoparticles are more exposed to the environment. Finally, the highest heating values found for $ION_{int-ext}$-HNT-3 suggest that the overall hyperthermal performance of the systems is (in first approximation) additive between internal and external particles.

4. Conclusions

A family of easily recoverable magnetic and thermally responsive composite materials, with nanoscale dimensions, were synthesized by a rapid and simple solvothermal approach, using MW irradiation to thermally activate the synthesis.

According to recent literature[76], the development of bifunctional composites as confined nano-catalysts represents an emerging research area, which is unexplored for phosphoric acid/halloysite inorganic mesoporous materials.The use of a confined nanoreactor with phosphorylated catalytic active sites thus enhanced the urea hydrolysis rate and therefore promoted the in-situ co-precipitation of iron oxide nanoparticles. HNTs-(H^+-PO_4) were found to be particularly suitable for the in-situ

cascade reactions of urea hydrolysis and iron nanoparticle deposition in mild MW-assisted reaction conditions.

The methodology proposed here proved to be highly versatile. It led to a good control of the reaction and to the selective functionalization of the inner or outer surfaces of the nanotubes with magnetic nanoparticles. Moreover, the composite nanomaterials are able of heating under a remotely applied magnetic field.

Two different protocols were used which only differ in the iron precursor. The first protocol uses $FeCl_2.4H_2O$ as the iron salt precursor. In the second, a green approach, with the pre-functionalization of the iron salt with clove essential oil as green reducing agent to give a eugenol EO-iron complex, led to the deposition of IONs on the inner surface of the nanotubes. It was therefore possible to selectively prepare different magnetic composites bearing ION particles in the inner lumen and/or outer surface which would thus be suitable for different uses such as carriers for drug delivery or as catalysts.

All the composites showed superparamagnetic behaviour at room temperature with magnetic properties influenced by the iron salt precursor. They were enhanced when the eugenol EO-iron complex was used in the synthesis. The magnetic nanocomposite showed textural, morphological and magnetic properties in line with the literature reports (which only accounts for conventional heating approaches[32–56]). Finally, the use of favourable energy systems such as microwave-assisted synthesis enabled high performance materials to be obtained in short synthesis times and using a simple methodology according to the principles of sustainable chemistry.

The observed superparamagnetic properties among with the promising heating characteristics of IONs make the synthesised IONs-HNTs potential nanocarriers for applications in antibacterial treatment and targeted hyperthermia therapy as recently proposed elsewhere[77,78].

CRediT authorship contribution statement

José Gonzalez-Rivera: Conceptualization, Investigation, Formal Analysis, Writing – original draft. Alessio Spepi: Investigation, Formal Analysis. Carlo Ferrari: Resources, Supervision, Writing – review and editing. Jorge Tovar-Rodriguez: Investigation, Formal Analysis. Elvira Fantechi: Investigation, Formal Analysis. Francesco Pineider: Investigation, Supervision, Writing – review and editing. Marco Antonio Vera-Ramirez: Investigation, Formal Analysis. Maria Rosaria Tiné: Conceptualization, Methodology, Resources, Supervision, Writing- Reviewing and Editing. Celia Duce: Resources, Supervision, Writing – review and editing.

Declaration of Competing Interest

The authors declare no conflict of interest.

Acknowledgments

This research is supported by the Advanced Green Materials for Cultural Heritage (AGM for CuHe) project (PNR fund with code: ARS01_00697; CUP E66C18000380005) and, Project INSOLE-Innovazioni agronomiche e tecnologiche per la coltivazione sostenibile di piante officinali e la produzione di oli essenziali di qualità" nell'ambito del PSR Sicilia 2014-2020. Sottomisura 16.1. Sostegno per la costituzione e la gestione di gruppi operativi del PEI in materia di produttività e sostenibilità dell'agricoltura. F. P. and E.F. acknowledge the financial support of PRA_2017_25 from the University of Pisa. The authors would like to thank Dr. Claudia Innocenti (ICCOM-CNR and Department of Chemistry “Ugo Schiff”, University of Florence) for the magnetic measurements and helpful discussions. The authors would also like to thank C. Lanza, A. Barbini and F. Pardini (INO-CNR) for their valuable technical support.

References

[1] Y. Zhang, A. Tang, H. Yang, J. Ouyang, Applications and interfaces of halloysite nanocomposites, Appl. Clay Sci. 119 (2016) 8–17. https://doi.org/10.1016/j.clay.2015.06.034.

[2] G. Cavallaro, L. Chiappisi, P. Pasbakhsh, M. Gradzielski, G. Lazzara, A structural comparison of halloysite nanotubes of di ff erent origin by Small- Angle Neutron Scattering (SANS) and Electric Birefringence, Appl. Clay Sci. 160 (2018) 71–80. https://doi.org/10.1016/j.clay.2017.12.044.

[3] E.A. Naumenko, I.D. Guryanov, R. Yendluri, Y.M. Lvov, R.F. Fakhrullin, Clay nanotube–biopolymer composite scaffolds for tissue engineering, Nanoscale. 8 (2016) 7257–7271. https://doi.org/10.1039/c6nr00641h.

[4] C. Duce, S. Vecchio, L. Ghezzi, V. Ierardi, M.R. Tiné, Thermal behavior study of pristine and modified halloysite nanotubes, J. Therm. Anal Calorim. 121 (2015) 1011–1019. https://doi.org/10.1007/s10973-015-4741-7.

[5] P. Yuan, D. Tan, F. Annabi-Bergaya, Properties and applications of halloysite nanotubes: recent research advances and future prospects, Appl. Clay Sci. 112–113 (2015) 75–93. https://doi.org/10.1016/j.clay.2015.05.001.

[6] M. Du, B. Guo, D. Jia, Newly emerging applications of halloysite nanotubes: A review, Polym. Int. 59 (2010) 574–582. https://doi.org/10.1002/pi.2754.

[7] G. Lazzara, G. Cavallaro, A. Panchal, R. Fakhrullin, A. Stavitskaya, V. Vinokurov, Y. Lvov, An assembly of organic-inorganic composites using halloysite clay nanotubes, Curr. Opin. Colloid Interface Sci. 35 (2018) 42–50. https://doi.org/10.1016/j.cocis.2018.01.002.

[8] M. Massaro, G. Barone, G. Biddeci, G. Cavallaro, F. Di, G. Lazzara, G. Nicotra, C. Spinella, G. Spinelli, S. Riela, Halloysite nanotubes-carbon dots hybrids multifunctional nanocarrier with positive cell target ability as a potential non-viral vector for oral gene therapy, J. Colloid Interface Sci. 552 (2019) 236–246. https://doi.org/10.1016/j.jcis.2019.05.062.

[9] G. Zhuang, M. Jaber, F. Rodrigues, B. Rigaud, P. Walter, Z. Zhang, A new durable pigment with hydrophobic surface based on natural nanotubes and indigo: Interactions and stability, J. Colloid Interface Sci. 552 (2019) 204–217. https://doi.org/10.1016/j.jcis.2019.04.072.

[10] L. Lisuzzo, G. Cavallaro, S. Milioto, G. Lazzara, Halloysite nanotubes filled with MgO for paper reinforcement and deacidification, Appl. Clay Sci. 213 (2021) 106231. https://doi.org/10.1016/j.clay.2021.106231.

[11] P. Cai, K. Di, J. Lv, S. Li, X. Chen, Environmentally benign and durable superhydrophobic coatings based on short fluorocarbon chain siloxane modified halloysite nanotubes for oil/water separation, Colloids Surfaces A Physicochem. Eng. Asp. 630 (2021) 127540. https://doi.org/10.1016/j.colsurfa.2021.127540.

[12] S. Kouser, A. Prabhu, K. Prashantha, G.K. Nagaraja, J. Neetha, K.M. Navada, A. Qurashi, D.J. Manasa, Colloids and Surfaces A : Modified halloysite nanotubes with Chitosan incorporated PVA / PVP bionanocomposite films : Thermal , mechanical properties and biocompatibility for tissue engineering, Colloids Surfaces A Physicochem. Eng. Asp. 634 (2022) 127941. https://doi.org/10.1016/j.colsurfa.2021.127941.

[13] A. Spepi, C. Duce, A. Pedone, D. Presti, J. González Rivera, V. Ierardi, M.R. Tinè, Experimental and DFT Characterization of Halloysite Nanotubes Loaded with Salicylic Acid, J. Phys. Chem. C. 120 (2016) 26759–26769. https://doi.org/10.1021/acs.jpcc.6b06964.

[14] L. Ghezzi, A. Spepi, M. Agnolucci, C. Cristani, M. Giovannetti, M.R. Tiné, C. Duce, Kinetics of release and antibacterial activity of salicylic acid loaded into halloysite nanotubes, Appl. Clay Sci. 160 (2018) 88–94. https://doi.org/10.1016/j.clay.2017.11.041.

[15] A. Stavitskaya, C. Shakhbazova, Y. Cherednichenko, L. Nigamatzyanova, G. Fakhrullina, N. Khaertdinov, G. Kuralbayeva, A. Filimonova, V. Vinokurov, R. Fakhrullin, Antibacterial properties and in vivo studies of tannic acid-stabilized silver–halloysite nanomaterials , Clay Miner. 55 (2020) 112–119. https://doi.org/10.1180/clm.2020.17.

[16] M. Massaro, R. Amorati, G. Cavallaro, S. Guernelli, G. Lazzara, S. Milioto, R. Noto, P. Poma, S. Riela, Direct chemical grafted curcumin on halloysite nanotubes as dual-responsive prodrug for pharmacological applications, Colloids Surfaces B Biointerfaces. 140 (2016) 505–513. https://doi.org/10.1016/j.colsurfb.2016.01.025.

[17] M. Massaro, G. Cavallaro, C.G. Colletti, G.D. Azzo, S. Guernelli, G. Lazzara, S. Pieraccini, S. Riela, Halloysite nanotubes for efficient loading , stabilization and controlled release of insulin, J. Colloid Interface Sci. 524 (2018) 156–164. https://doi.org/10.1016/j.jcis.2018.04.025.

[18] S. Ghalei, S. Hopkins, M. Douglass, M. Garren, A. Mondal, H. Handa, Nitric oxide releasing halloysite nanotubes for biomedical applications, J. Colloid Interface Sci. 590 (2021) 277–289. https://doi.org/10.1016/j.jcis.2021.01.047.

[19] H. Jing, Y. Higaki, W. Ma, H. Wu, W.O. Yah, H. Otsuka, Y.M. Lvov, A. Takahara, Internally Modified Halloysite Nanotubes as Inorganic Nanocontainers for a Flame Retardant, Chem. Lett. 42 (2013) 121–123. https://doi.org/10.1246/cl.2013.121.

[20] P. Xu, C. Wang, B. Zhao, Y. Zhou, H. Cheng, An interfacial coating with high corrosion resistance based on halloysite nanotubes for anode protection of zinc-ion batteries, J. Colloid Interface Sci. 602 (2021) 859–867. https://doi.org/10.1016/j.jcis.2021.06.057.

[21] M. Massaro, S. Riela, G. Lazzara, M. Gruttadauria, S. Milioto, R. Noto, Green conditions for the Suzuki reaction using microwave irradiation and a new HNT-supported ionic liquid-like phase (HNT-SILLP) catalyst, Appl. Organomet. Chem. 28 (2014) 234–238. https://doi.org/10.1002/aoc.3114.

[22] N. Bahri-laleh, S. Sadjadi, A. Poater, Pd immobilized on dendrimer decorated halloysite clay: Computational and experimental study on the effect of dendrimer generation , Pd valance and incorporation of terminal functionality on the catalytic activity, J. Colloid Interface Sci. 531 (2018) 421–432. https://doi.org/10.1016/j.jcis.2018.07.039.

[23] Z. He, H. Wang, M. Li, L. Feng, J. Niu, Z. Li, X. Jia, G. Hu, Amorphous cobalt oxide decorated halloysite nanotubes for efficient sulfamethoxazole degradation activated by peroxymonosulfate, J. Colloid Interface Sci. (2021). https://doi.org/10.1016/j.jcis.2021.08.168.

[24] A. V. Stavitskaya, E.A. Kozlova, A.Y. Kurenkova, A.P. Glotov, D.S. Selischev, E. V. Ivanov, D. V. Kozlov, V.A. Vinokurov, R.F. Fakhrullin, Y.M. Lvov, Ru/CdS Quantum Dots Templated on Clay Nanotubes as Visible-Light-Active Photocatalysts: Optimization of S/Cd Ratio and Ru Content, Chem. - A Eur. J. 26 (2020) 13085–13092.

https://doi.org/10.1002/chem.202002192.
[25] A. Stavitskaya, G. Fakhrullina, L. Nigamatzyanova, E. Sitmukhanova, E. Khusnetdenova, R. Fakhrullin, V. Vinokurov, Biodistribution of quantum dots-labelled halloysite nanotubes: A caenorhabditis elegans in vivo study, Materials (Basel). 14 (2021) 1–10. https://doi.org/10.3390/ma14195469.
[26] Y. Zhang, Y. Xie, A. Tang, Y. Zhou, J. Ouyang, H. Yang, Precious-metal nanoparticles anchored onto functionalized halloysite nanotubes, Ind. Eng. Chem. Res. 53 (2014) 5507–5514. https://doi.org/10.1021/ie404326j.
[27] M. V. Gorbachevskii, A. V. Stavitskaya, A.A. Novikov, R.F. Fakhrullin, E. V. Rozhina, E.A. Naumenko, V.A. Vinokurov, Fluorescent gold nanoclusters stabilized on halloysite nanotubes: in vitro study on cytotoxicity, Appl. Clay Sci. 207 (2021) 106106. https://doi.org/10.1016/j.clay.2021.106106.
[28] O. Owoseni, E. Nyankson, Y. Zhang, D.J. Adams, J. He, L. Spinu, G.L. McPherson, A. Bose, R.B. Gupta, V.T. John, Interfacial adsorption and surfactant release characteristics of magnetically functionalized halloysite nanotubes for responsive emulsions, J. Colloid Interface Sci. 463 (2016) 288–298. https://doi.org/10.1016/j.jcis.2015.10.064.
[29] W. Ma, J. Dai, X. Dai, Z. Da, Y. Yan, Preparation and characterization of chitosan/halloysite magnetic microspheres and their application for removal of tetracycline from an aqueous solution, Desalin. Water Treat. 57 (2016) 4162–4173. https://doi.org/10.1080/19443994.2014.988653.
[30] S. Dolci, V. Domenici, C. Duce, M.R. Tiné, V. Ierardi, U. Valbusa, Z. Jaglicic, A. Boni, M. Gemmi, G. Pampaloni, Ultrasmall superparamagnetic iron oxide nanoparticles with titanium-N,N-dialkylcarbamato coating, Mater. Res. Express. 1 (2014) 035401. https://doi.org/10.1088/2053-1591/1/3/035401.
[31] A. Spepi, C. Duce, C. Ferrari, J. González-Rivera, Z. Jagličić, V. Domenici, F. Pineider, M.R. Tiné, A simple and versatile solvothermal configuration to synthesize superparamagnetic iron oxide nanoparticles using a coaxial microwave antenna, RSC Adv. 6 (2016) 104366–104374. https://doi.org/10.1039/c6ra17513a.
[32] P. Zheng, Y. Du, X. Ma, Selective fabrication of iron oxide particles in halloysite lumen, Mater. Chem. Phys. 151 (2015) 14–17. https://doi.org/10.1016/j.matchemphys.2014.11.075.
[33] Y. Xie, D. Qian, D. Wu, X. Ma, Magnetic halloysite nanotubes/iron oxide composites for the adsorption of dyes, Chem. Eng. J. 168 (2011) 959–963. https://doi.org/10.1016/j.cej.2011.02.031.
[34] M. Amjadi, A. Samadi, J.L. Manzoori, A composite prepared from halloysite nanotubes and magnetite (Fe3O4) as a new magnetic sorbent for the preconcentration of cadmium(II) prior to its determination by flame atomic absorption spectrometry, Microchim. Acta. 182 (2015) 1627–1633. https://doi.org/10.1007/s00604-015-1491-y.
[35] L. Jiang, C. Zhang, J. Wei, W. Tjiu, J. Pan, Y. Chen, T. Liu, Surface modifications of halloysite nanotubes with superparamagnetic Fe3O4 nanoparticles and carbonaceous layers for efficient adsorption of dyes in water treatment, Chem. Res. Chinese Univ. 30 (2014) 971–977. https://doi.org/10.1007/s40242-014-4218-4.
[36] B. Mu, W. Zhang, A. Wang, Facile fabrication of superparamagnetic coaxial gold/halloysite nanotubes/Fe3O4 nanocomposites with excellent catalytic property for 4-nitrophenol reduction, J. Mater. Sci. 49 (2014) 7181–7191.

https://doi.org/10.1007/s10853-014-8426-6.
[37] A.-B. Zhang, S.-T. Liu, K.-K. Yan, Y. Ye, X.-G. Chen, Facile preparation of MnFe2O4/halloysite nanotubular encapsulates with enhanced magnetic and electromagnetic performances, RSC Adv. 4 (2014) 13565. https://doi.org/10.1039/c3ra46873a.
[38] J. Duan, R. Liu, T. Chen, B. Zhang, J. Liu, Halloysite nanotube-Fe3O4 composite for removal of methyl violet from aqueous solutions, Desalination. 293 (2012) 46–52. https://doi.org/10.1016/j.desal.2012.02.022.
[39] A.B. Ganganboina, A.D. Chowdhury, R. Doong, Nano assembly of N-doped graphene quantum dots anchored Fe3O4/halloysite nanotubes for high performance supercapacitor, Electrochim. Acta. 245 (2017) 912–923. https://doi.org/10.1016/j.electacta.2017.06.002.
[40] M. Kim, S.C. Jee, J. Sung, A.A. Kadam, Anti-proliferative applications of laccase immobilized on super-magnetic chitosan-functionalized halloysite nanotubes, Int. J. Biol. Macromol. 118 (2018) 228–237. https://doi.org/10.1016/j.ijbiomac.2018.06.074.
[41] Y. Lee, S. Lee, S.C. Jee, J. Sung, A.A. Kadam, Surface functionalization of halloysite nanotubes with supermagnetic iron oxide , chitosan and 2-D calcium-phosphate nano flakes for synergistic osteoconduction enhancement of human adipose tissue-derived mesenchymal stem cells, Colloids Surfaces B Biointerfaces. 173 (2019) 18–26. https://doi.org/10.1016/j.colsurfb.2018.09.045.
[42] Y. Zhang, H. Yang, Halloysite nanotubes coated with magnetic nanoparticles, Appl. Clay Sci. 56 (2012) 97–102. https://doi.org/10.1016/j.clay.2011.11.028.
[43] R. Riahi-madvaar, M.A. Taher, H. Fazelirad, Synthesis and characterization of magnetic halloysite-iron oxide nanocomposite and its application for naphthol green B removal, Appl. Clay Sci. 137 (2017) 101–106. https://doi.org/10.1016/j.clay.2016.12.019.
[44] D. Janacek, L. Kvitek, M. Karlikova, K. Pospiskova, I. Safarik, Removal of silver nanoparticles with native and magnetically modified halloysite, Appl. Clay Sci. 162 (2018) 10–14. https://doi.org/10.1016/j.clay.2018.05.024.
[45] J. Dai, X. Wei, Z. Cao, Z. Zhou, P. Yuc, J. Pan, T. Zou, C. Li, Y. Yan, Highly-controllable imprinted polymer nanoshell at the surface of magnetic halloysite nanotubes for selective recognition and rapid adsorption of tetracycline, RSC Adv. 4 (2014) 7967–7978.
[46] X. Zeng, Z. Sun, H. Wang, Q. Wang, Y. Yang, Supramolecular gel composites reinforced by using halloysite nanotubes loading with in-situ formed Fe3O4 nanoparticles and used for dye adsorption, Compos. Sci. Technol. 122 (2016) 149–154. https://doi.org/10.1016/j.compscitech.2015.11.025.
[47] M. Fayazi, M.A. Taher, D. Afzali, A. Mostafavi, Fe3O4 and MnO2 assembled on halloysite nanotubes : A highly efficient solid-phase extractant for electrochemical detection of mercury (II) ions, Sensors Actuators B. Chem. 228 (2016) 1–9. https://doi.org/10.1016/j.snb.2015.12.107.
[48] R. Abhinayaa, G. Jeevitha, D. Mangalaraj, N. Ponpandian, K. Vidhya, J. Angayarkanni, Cytotoxic consequences of Halloysite nanotube/iron oxide nanocomposite and iron oxide nanoparticles upon interaction with bacterial , non-cancerous and cancerous cells, Colloids Surfaces B Biointerfaces. 169 (2018) 395–403. https://doi.org/10.1016/j.colsurfb.2018.05.040.

[49] X. Song, L. Zhou, Y. Zhang, P. Chen, Z. Yang, A novel cactus-like Fe3O4/Halloysite nanocomposite for arsenite and arsenate removal from water, J. Clean. Prod. 224 (2019) 573–582. https://doi.org/10.1016/j.jclepro.2019.03.230.

[50] P. Maziarz, J. Matusik, T. Leiviskä, T. Straczek, C. Kapusa, W.W. Woch, W. Tokarz, K. Górniak, Toward highly effective and easily separable halloysite-containing adsorbents : The effect of iron oxide particles impregnation and new insight into As (V) removal mechanisms, Sep. Purif. Technol. 210 (2019) 390–401. https://doi.org/10.1016/j.seppur.2018.08.012.

[51] K. Zhu, Y. Duan, F. Wang, P. Gao, H. Jia, C. Ma, C. Wang, Silane-modified halloysite/Fe3O4 nanocomposites: Simultaneous removal of Cr(VI) and Sb(V) and positive effects of Cr(VI) on Sb (V) adsorption, Chem. Eng. J. 311 (2017) 236–246. https://doi.org/10.1016/j.cej.2016.11.101.

[52] T. Tsoufis, F. Katsaros, B.J. Kooi, E. Bletsa, S. Papageorgiou, Y. Deligiannakis, I. Panagiotopoulos, Halloysite nanotube-magnetic iron oxide nanoparticle hybrids for the rapid catalytic decomposition of pentachlorophenol, Chem. Eng. J. 313 (2017) 466–474. https://doi.org/10.1016/j.cej.2016.12.056.

[53] D. Afzali, M. Fayazi, Deposition of MnO2 nanoparticles on the magnetic halloysite nanotubes by hydrothermal method for lead (II) removal from aqueous solutions, J. Taiwan Inst. Chem. Eng. 63 (2016) 421–429. https://doi.org/10.1016/j.jtice.2016.02.025.

[54] H. Fu, L. Liao, X. Li, W. Chen, Preparation and characterization of novel modified halloysite-Fe3O4-Ag/polyurea nanocomposites with antibacterial property, Int. J. Polym. Mater. Polym. Biomater. 65 (2016) 863–871.

[55] T. Zhou, L. Jia, Y.-F. Luo, J. Xu, R.-H. Chen, Z. Ge, T. Ma, T. Zhu, Multifunctional nanocomposite based on halloysite nanotubes for efficient luminescent bioimaging and magnetic resonance imaging, Int. J. Nanomedicine. 11 (2016) 4765–4776.

[56] E. Rozhina, S. Batasheva, M. Gomzikova, E. Naumenko, R. Fakhrullin, Multicellular spheroids formation : The synergistic effects of halloysite nanoclay and cationic magnetic nanoparticles, Colloids Surfaces A. 565 (2019) 16–24. https://doi.org/10.1016/j.colsurfa.2018.12.038.

[57] S.A. Konnova, Y.M. Lvov, R.F. Fakhrullin, Magnetic halloysite nanotubes for yeast cell surface engineering, Clay Miner. 51 (2016) 429–433. https://doi.org/10.1180/claymin.2016.051.3.07.

[58] J. González-Rivera, A. Spepi, C. Ferrari, I. Longo, J. Tovar, E. Fantechi, C. Innocenti, F. Pineider, M.A. Vera-ramírez, M. Rosaria, C. Duce, Structural , textural and thermal characterization of a confined nanoreactor with phosphorylated catalytic sites grafted onto a halloysite nanotube lumen, Appl. Clay Sci. 196 (2020) 105752. https://doi.org/10.1016/j.clay.2020.105752.

[59] J. González-Rivera, I.R. Galindo-Esquivel, M. Onor, E. Bramanti, I. Longo, C. Ferrari, Heterogeneous catalytic reaction of microcrystalline cellulose in hydrothermal microwave-assisted decomposition: effect of modified zeolite Beta, Green Chem. 16 (2014) 1417–1425. https://doi.org/10.1039/c3gc42207k.

[60] I. Longo, A.S. Ricci, Chemical activation using an open-end coaxial applicator, J. Microw. Power Electromagn. Energy. 41 (2007) 4–19.

[61] B. Campanella, J.G. Rivera, C. Ferrari, S. Biagi, M. Onor, A. D'Ulivo, E. Bramanti,

Microwave photochemical reactor for the online oxidative decomposition of p-hydroxymercurybenzoate (pHMB)-tagged proteins and their determination by cold vapor generation-atomic fluorescence detection., Anal. Chem. 85 (2013) 12152–7. https://doi.org/10.1021/ac403389z.

[62] J. González-Rivera, C. Duce, V. Ierardi, I. Longo, A. Spepi, M.R. Tiné, C. Ferrari, Fast and Eco-friendly Microwave-Assisted Synthesis of Silver Nanoparticles using Rosemary Essential Oil as Renewable Reducing Agent., ChemistrySelect. 2 (2017) 2131–2138. https://doi.org/10.1002/slct.201700244.

[63] J.S. Mondragon-Ochoa, J. González-Rivera, C. Toparli, R. Khanum, R.S. Moirangthem, C. Duce, C. Ferrari, G. Barillaro, A. Erbe, Microwave-assisted in situ laser dye incorporation into high sensitivity whispering gallery mode microresonators, J. Phys. D Appl. Phys. (2021) 0–12. https://doi.org/https://doi.org/10.1088/1361- 6463/ac2e34 Manuscript.

[64] J. González-Rivera, J. Tovar-Rodríguez, E. Bramanti, C. Duce, I. Longo, E. Fratini, I.R. Galindo-Esquivel, C. Ferrari, Surfactant recovery from mesoporous metal-modified materials (Sn–, Y–, Ce–, Si–MCM-41), by ultrasound assisted ion-exchange extraction and its re-use for a microwave in situ cheap and eco-friendly MCM-41 synthesis, J. Mater. Chem. A. 2 (2014) 7020–7033. https://doi.org/10.1039/c3ta15078j.

[65] F.N. Sayed, V. Polshettiwar, Facile and sustainable synthesis of shaped iron oxide nanoparticles: effect of iron precursor salts on the shapes of iron oxides., Sci. Rep. 5 (2015) 9733. https://doi.org/10.1038/srep09733.

[66] L. Lisuzzo, G. Cavallaro, P. Pasbakhsh, S. Milioto, G. Lazzara, Why does vacuum drive to the loading of halloysite nanotubes? The key role of water confinement, J. Colloid Interface Sci. 547 (2019) 361–369. https://doi.org/10.1016/j.jcis.2019.04.012.

[67] J. Gonzalez-Rivera, C. Duce, D. Falconieri, C. Ferrari, L. Ghezzi, A. Piras, M.R. Tine, Coaxial microwave assisted hydrodistillation of essential oils from five different herbs (lavender, rosemary, sage, fennel seeds and clove buds): Chemical composition and thermal analysis, Innov. Food Sci. Emerg. Technol. 33 (2016) 308–318. https://doi.org/10.1016/j.ifset.2015.12.011.

[68] J. Gonzalez-Rivera, C. Duce, B. Campanella, L. Bernazzani, C. Ferrari, E. Tanzini, M. Onor, I. Longo, J. Cabrera Ruiz, M.R. Tine, E. Bramanti, In situ microwave assisted extraction of clove buds to isolate essential oil, polyphenols, and lignocellulosic compounds, Ind. Crops Prod. 161 (2021). https://doi.org/10.1016/j.indcrop.2020.113203.

[69] I. Blanco, V. Siracusa, The use of thermal techniques in the characterization of bio-sourced polymers, Materials (Basel). 14 (2021) 1686. https://doi.org/10.3390/ma14071686.

[70] B. Brooks, W.A. Jessup, B.W. MacArthur, W.B. Sheats, Apparatus for quantitatively converting urea to ammonia on demand, US 20040208813A1, 2004.

[71] A.M. Grumezescu, B. Ş Vasile, A.M. Holban, Eugenol functionalized magnetite nanostructures used in anti-infectious therapy, Lett. Appl. Nanobioscience. 2 (2013) 120–123.

[72] N. Lee, D. Yoo, D. Ling, M.H. Cho, T. Hyeon, J. Cheon, Iron Oxide Based Nanoparticles for Multimodal Imaging and Magnetoresponsive Therapy, Chem. Rev. 115 (2015) 10637–10689. https://doi.org/10.1021/acs.chemrev.5b00112.

[73] S.R. Yassine, Z. Fatfat, G.H. Darwish, P. Karam, Localized catalysis driven by the induction heating of magnetic nanoparticles, Catal. Sci. Technol. 10 (2020) 3890–3896.

https://doi.org/10.1039/d0cy00439a.

[74] R. Hergt, S. Dutz, Magnetic particle hyperthermia-biophysical limitations of a visionary tumour therapy, J. Magn. Magn. Mater. 311 (2007) 187–192. https://doi.org/10.1016/j.jmmm.2006.10.1156.

[75] E. Fantechi, C. Innocenti, M. Zanardelli, M. Fittipaldi, E. Falvo, M. Carbo, V. Shullani, L. Di Cesare Mannelli, C. Ghelardini, A.M. Ferretti, A. Ponti, C. Sangregorio, P. Ceci, A smart platform for hyperthermia application in cancer treatment: Cobalt-doped ferrite nanoparticles mineralized in human ferritin cages, ACS Nano. 8 (2014) 4705–4719. https://doi.org/10.1021/nn500454n.

[76] L. Lisuzzo, G. Cavallaro, S. Milioto, G. Lazzara, Halloysite nanotubes as nanoreactors for heterogeneous micellar catalysis, J. Colloid Interface Sci. 608 (2021) 424–434. https://doi.org/10.1016/j.jcis.2021.09.146.

[77] A. V. Kornilova, G.A. Kuralbayeva, A. V. Stavitskaya, M. V. Gorbachevskii, O. V. Karpukhina, I. V. Lysenko, V. V. Pryadun, A.A. Novikov, A.N. Vasiliev, V.Y. Timoshenko, Gold nanoparticles immobilized on halloysite nanotubes for spatially-temporally localized photohyperthermia, Appl. Surf. Sci. 566 (2021) 150671. https://doi.org/10.1016/j.apsusc.2021.150671.

[78] X. Luo, J. Zhang, Y.P. Wu, X. Yang, X.P. Kuang, W.X. Li, Y.F. Li, R.R. He, M. Liu, Multifunctional HNT@Fe3O4@PPy@DOX Nanoplatform for Effective Chemo-Photothermal Combination Therapy of Breast Cancer with MR Imaging, ACS Biomater. Sci. Eng. 6 (2020) 3361–3374. https://doi.org/10.1021/acsbiomaterials.9b01709.